5-12-2015

The 2d Distribution of Iron-Rich Ejecta in the Remnant of SN 1885 in M31

Robert A. Fesen
Dartmouth College

Peter A. Höflich
Florida State University

Andrew J. S. Hamilton
University of Colorado

The Astrophysical Journal, 804:140 (13pp), 2015 May 10 doi:10.1088/0004-637X/804/2/140

THE 2D DISTRIBUTION OF IRON-RICH EJECTA IN THE REMNANT OF SN 1885 IN M31*

Robert A. Fesen[1], Peter A. Höflich[2], and Andrew J. S. Hamilton[3]
[1] Department of Physics & Astronomy, Dartmouth College, 6127 Wilder Lab, Hanover, NH 03755, USA
[2] Department of Physics, Florida State University, Tallahassee, FL 32306, USA
[3] JILA and the Department of Astrophysical and Planetary Sciences, University of Colorado, Boulder, CO 80309, USA
Received 2014 December 9; accepted 2015 March 4; published 2015 May 12

ABSTRACT

We present *Hubble Space Telescope* (*HST*) ultraviolet Fe I and Fe II images of the remnant of Supernova 1885 (S And) which is observed in absorption against the bulge of the Andromeda galaxy, M31. We compare these Fe I and Fe II absorption line images to previous *HST* absorption images of S And, of which the highest quality and theoretically cleanest is Ca II H and K. Because the remnant is still in free expansion, these images provide a 2D look at the distribution of iron synthesized in this probable Type Ia explosion, thus providing insights and constraints for theoretical SN Ia models. The Fe I images show extended absorption offset to the east from the remnant's center as defined by Ca II images and is likely an ionization effect due to self-shielding. More significant is the remnant's apparent Fe II distribution which consists of four streams or plumes of Fe-rich material seen in absorption that extend from remnant center out to about 10,000 km s^{-1}. This is in contrast to the remnant's Ca II absorption, which is concentrated in a clumpy, broken shell spanning velocities of 1000–5000 km s^{-1} but which extends out to 12,500 km s^{-1}. The observed distributions of Ca- and Fe-rich ejecta in the SN 1885 remnant are consistent with delayed detonation white dwarf models. The largely spherical symmetry of the Ca-rich layer argues against a highly anisotropic explosion as might result from a violent merger of two white dwarfs.

Key words: ISM: abundances – ISM: kinematics and dynamics – ISM: supernova remnants – supernovae: general – supernovae: individual (SN 1885)

1. INTRODUCTION

The prevailing picture of common Type Ia supernovae (SNe Ia) is that they are explosions of degenerate carbon–oxygen white dwarfs that undergo a thermonuclear runaway when they reach the Chandrasekhar limit as a result of mass transfer in some type of close binary stellar system (Hoyle & Fowler 1960; Colgate & McKee 1969; Nomoto et al. 1984; Hillebrandt & Niemeyer 2000; Li et al. 2003). Two categories of progenitor systems are considered promising: a "single degenerate" system comprising a single white dwarf that accretes from a companion main sequence, helium, or red giant star (Branch et al. 1995; Nomoto et al. 2003; Di Stefano et al. 2011; Wang & Han 2012) and a "double degenerate" system in which two white dwarfs merge after losing angular momentum by gravitational radiation (Iben & Tutukov 1984; Webbink 1984). The diversity of observed SNe Ia suggests that more than a single scenario may operate (Höflich & Khokhlov 1996; Quimby et al. 2006; Hillebrandt et al. 2013). Possible SN Ia progenitor systems have been discussed recently by Howell (2011), Nugent et al. (2011), Bloom et al. (2012), Di Stefano & Kilic (2012), and Höflich et al. (2013).

The mechanism by which the explosion proceeds in white dwarfs remains poorly understood. Thermonuclear runaway models involving a pure detonation (a supersonic shock wave) appear to be ruled out because they predict that the white dwarf would be nearly entirely incinerated to iron-group elements, chiefly ^{56}Ni, whereas observed spectra of SNe Ia show substantial quantities of intermediate mass elements. Similarly, models involving a pure deflagration (a subsonic burning wave) are ruled out because the convectively unstable deflagration front effectively mixes all elements radially, whereas observed spectra and light curves suggest a layered structure with intermediate mass elements on the outside and nickel–iron on the inside.

Khokhlov (1991) proposed that SN Ia light curves could be explained empirically by a "delayed detonation" scenario in which the explosion starts in the core as a deflagration wave, which is followed somehow by a detonation wave of overlying unburned material which unbinds the white dwarf completely. Heat conduction from the initial deflagration front pre-heats and expands the star's outer layers, lifting their electron degeneracy so that when those outer layers subsequently detonate, their explosion is softened. The consequence is that burning of the outer layers does not continue to completion, and a layered structure of intermediate mass elements is produced like that observed.

Numerical calculations indicate that the thermonuclear runaway of a near Chandrasekhar-mass white dwarf is preceded by a century long, highly turbulent, convective, carbon-burning, "smoldering" phase (Sugimoto & Nomoto 1980; Nomoto 1982; Hillebrandt & Niemeyer 2000). Ignition, which occurs at around 1.5 × 10^9 K, is highly sensitive to temperature and density and may occur off-center and proceed along paths of least resistance determined by the fluctuating conditions around the ignition point (Timmes & Woosley 1992; Garcia-Senz & Woosley 1995; Niemeyer et al. 1996; Höflich & Stein 2002; Livne et al. 2005).

Recent three-dimensional numerical simulations suggest that deflagration may proceed along a single dominant plume that starts off-center and breaks through to the surface of the white dwarf (Plewa 2007). While hydrodynamical calculations during the deflagration phase depend sensitively on the initial conditions at the time of the thermonuclear runaway, some calculations suggest strong mixing of partially and complete

* Based on observations with the NASA/ESA *Hubble Space Telescope*, obtained at the Space Telescope Science Institute, which is operated by the Association of Universities for Research in Astronomy, Inc. under NASA contract No. NAS5-26555.

burning products throughout the white dwarf (WD) (Gamezo et al. 2003; Röpke et al. 2006).

SN Ia explosion computations are quite challenging, involving a complex interplay of turbulent hydrodynamics, nuclear burning, conduction, radiative transfer in iron-group rich material, and perhaps magnetic fields leading to uncertainties (Khokhlov 1995; Niemeyer & Hillebrandt 1995; Livne 1999; Reinecke et al. 1999; Gamezo et al. 2004; Röpke et al. 2012). Several key questions about expansion asymmetries and the overall characteristics of SNe Ia could be resolved if one could obtain direct observations of the distribution and kinematics of elements in young SN Ia remnants.

However, freely expanding ejecta cool adiabatically, thereby becoming faint and effectively invisible via line emission in just a few years. Nonetheless, as long as a remnant's ejecta are still in the free expansion phase, the velocity distribution of elements remains essentially the same as that established shortly after the explosion.

Fortunately, such an investigation is possible for SN 1885, the bright historical nova known as S Andromeda (S And). S And was discovered in late August of 1885 located at a projected distance just 16″ away from M31's nucleus. Because of its central location in M31, the remnant's expanding ejecta is visible not by emission, but via resonance line absorption against the background of the Andromeda galaxy's bulge stars. SN 1885's reported optical spectrum lacked hydrogen lines, defining it as Type I (de Vaucouleurs & Corwin 1985). Its reddish appearance and fast light curve suggests a subluminous Type Ia event (de Vaucouleurs & Corwin 1985) although this classification is uncertain (see Chevalier & Plait 1988; Pastorello et al. 2008; Perets et al. 2011).

Numerous searches for the remnant of SN 1885 in emission failed for nearly a century (e.g., those of W. Baade discussed by Osterbrock 2001). The remnant was finally detected through a ground-based, near-ultraviolet (near-UV) image which revealed a small dark spot of Ca and Fe resonance line absorption silhouetted against the starry background of M31's bulge (Fesen et al. 1989).

Follow-up images taken with the *Hubble Space Telescope* (*HST*) revealed a circular ≃0.″75 diameter dark spot produced by a blend of Ca II H and K line absorption (Fesen et al. 1999). Subsequent UV imaging of the remnant with *HST* using the WFC2 F255W filter revealed a 0.″5 diameter absorption spot likely due largely to saturated UV Fe II resonance lines (Hamilton & Fesen 2000).

Spectra taken with Faint Object Spectrograph (FOS) on *HST* established that the absorption was produced principally by Ca II K & H 3934,3968 Å, with additional contributions from Ca I 4227 and Fe I 3720,3441 Å (Fesen et al. 1999). The remnant's Ca II absorption was found to extend to a maximum velocity of ≃13,100 ± 1500 km s^{-1}. The strength of the Fe I 3720 absorption line, the relative strengths of Ca I and Ca II lines, and the depth of the imaged Fe II absorption spot were used to estimate an iron mass (in the form of Fe II) between 0.1 to 1.0 $M_{\odot}$.

Narrow passband images taken in 2004 with the Wide Field Channel of the Advanced Camera for Surveys (ACS/WFC) on *HST* showed that the Ca II absorption is roughly spherical with a maximum diameter of 0.″8 (Fesen et al. 2007). At the known distance 785 ± 25 kpc of M31 (McConnachie et al. 2005), this angular diameter corresponds to a mean expansion velocity of 12,500 km s^{-1} over the ≃120 yr age of SN 1885. The agreement between the remnant's size and its expansion velocity as measured in the Ca II absorption implies that the SN 1885 remnant is still virtually in free expansion. This is also consistent with the fact that the remnant is an exceptionally weak radio source (Sjouwerman & Dickel 2001; Hofmann et al. 2013) with no confirmed X-ray emission (Kaaret 2002).

Since its ejecta are in free expansion, the distribution of elements is essentially the same as that shortly after the explosion. The dominant element near the center of the remnant at the present time is expected to be iron, and the dominant iron ionization species is expected to be Fe II. The presence of Fe I in the FOS spectrum attests to the relatively low ionization state of the supernova ejecta in general. The photoionization timescale of Fe I exposed to the observed flux of UV light from the bulge of M31 is of order 10 yr (Fesen et al. 1999). The fact that Fe I is still present can be attributed to partial self-shielding by its own continuum optical depth.

Although Fe II is expected to be the dominant ion of iron, imaging the remnant's iron-rich material via Fe II absorption is challenging. This is because the bulge of M31 is faint at the wavelengths ∼2500 Å of the strongest near-UV Fe II absorption lines. A detection of SN 1885 in Fe II using the WFPC2 on *HST* was reported by Hamilton & Fesen (2000) but the remnant was barely resolved with a low signal-to-noise ratio (S/N).

The Wide Field Planetary Camera 3 for UV and optical imaging (WFP3/UVIS) installed on *HST* in 2009 is significantly more sensitive than its precursors, WFPC2 and ACS. Here we present a spatially resolved, long exposure image of the 2D distribution of Fe II in SN 1885 obtained with WFPC3. The WFC3/UVIS filter F225W, covers the strong 2344 and 2383 Å resonance lines of Fe II and is largely free of contamination of absorption lines from lighter elements. We compare this image to other *HST* images of SN 1885, including Fe I images, and we discuss the implications of these data for explosion models of Type Ia. The observations and results are described in Sections 2 and 3, and the implications are discussed in Section 4. A summary of the findings and conclusions is given in Section 5.

2. OBSERVATIONS

Table 1 lists the *HST* images taken or examined as part of this study of the remnant of SN 1885, hereafter referred to as supernova remnant (SNR) 1885. These images were scaled and co-aligned using SAOimage and IRAF image routines applied to M31 bulge stars detected near the remnant.

The images were obtained using either the ACS Wide Field Channel (ACS/WFC), the ACS High Resolution Channel (ACS/HRC), or the WFC3/UVIS camera. The ACS/WFC detector consists of two 2048 × 4096 CCDs covering a field of view 202″ × 202″ with an average pixel size of 0.″05. The ACS/HRC consists of a single 1024 × 1024 CCD providing a spatial resolution of 0.″025 × 0.″025 pixel^{-1} and a nominal 29″ × 26″ field of view. The WFC3/UVIS detector has two 2051 × 4096 devices yielding a field of view of 162″ × 162″ with 0.″039 pixels.

Figure 1 (top panel) shows a model predicted UV-optical absorption spectrum of SNR 1885 (Fesen et al. 1999). Vertical lines, with lengths proportional to oscillator strengths, mark wavelengths of the strongest lines. For simplicity, all ions are assumed to have the same velocity profile as the observed Ca lines.

Table 1
Log of *HST* Images of the Remnant of SN 1885 in M31

HST Instrument	UT Date	Observation ID	Exposure Time (s)	Filter ID	Central Wavelength	Program ID	Comment
ACS/HRC	2004 Nov 20	J8ZS05010	15600	F250W	2716 Å	10118	Fe I, Fe II, Mg I & Mg II
ACS/HRC	2004 Oct 13	J8ZS04010	5200	F330W	3363 Å	10118	UV continuum
ACS/WFC	2009 Dec 14	JB2701010	12700	FR388N	3724 Å	11722	Fe I 3720 Å
ACS/WFC	2004 Nov 08	J8ZS03010	8960	FR388N	3951 Å	10118	Ca II H and K
ACS/WFC	2004 Nov 02	J8ZS02010	8960	FR423N	4227 Å	10118	Ca I 4227 Å
ACS/WFC	2004 Aug 25	J8ZS01010	4668	FR462N	4600 Å	10118	blue continuum
WFC3/UVIS	2012 Nov 18	IBR801010	8064	F225W	2366 Å	12609	Fe I & Fe II
WFC3/UVIS	2012 Nov 21	IBR802010	8064	F225W	2366 Å	12609	" "
WFC3/UVIS	2012 Dec 01	IBR803010	8064	F225W	2366 Å	12609	" "
WFC3/UVIS	2010 Jul 21	IBF310040	925	F275W	2707 Å	12058	Fe I, Fe II, Mg I & Mg II
WFC3/UVIS	2010 Jul 23	IBF311040	925	F275W	2707 Å	12058	" " " "
WFC3/UVIS	2010 Jul 21	IBF310030	1250	F336W	3355 Å	12058	UV continuum
WFC3/UVIS	2010 Jul 23	IBF311030	1250	F336W	3355 Å	12058	" "
WFC3/UVIS	2012 Dec 01	IBR803020	2724	F336W	3355 Å	12609	" "
WFC3/UVIS	2010 Dec 21	IBIR01020	2700	F373N	3730 Å	12174	Fe I 3720 Å
WFC3/UVIS	2010 Dec 25	IBIR06020	2700	F390M	3897 Å	12174	Ca II H and K
WFC3/UVIS	2010 Dec 23	IBIR05020	2700	F502N	5010 Å	12174	[O III] 5007 Å
WFC3/UVIS	2010 Dec 26	IBIR07020	2700	F547M	5447 Å	12174	V band
WFC3/UVIS	2010 Dec 21	IBIR02020	2700	F656N	6561 Å	12174	Hα 6563 Å
WFC3/UVIS	2010 Dec 21	IBIR03020	2700	F658N	6584 Å	12174	[N II] 6584 Å
WFC3/UVIS	2011 Jan 02	IBIR08020	2700	F665N	6650 Å	12174	Hα off-band

The model spectrum for SNR 1885 shown here differs slightly from that shown in Figure 4 of Fesen et al. (1999) in that the spectrum shown here is for a narrow line of sight through the center of the remnant, whereas the spectrum in Fesen et al. (1999) was convolved through the 0.″43 aperture of the FOS. Consequently the absorption lines here are slightly broader and deeper.

The strengths of Ca II, Ca I, and Fe I absorptions are from a fit to the FOS spectrum, while abundances of other elements are from the delayed detonation model of Höflich et al. (1998). All ions are assumed neutral or singly ionized, with the ratio of neutral to singly ionized being determined by the lifetime of the neutral against photoionization by UV light from the bulge of M31 (Fesen et al. 1999).

The middle plot of Figure 1 shows the transmission bandpasses for the WFC3/UVIS F225W, F275W, F336W, and F390M filters, along with the ACS/HRC F250W and ramp FR388N filters. The filter peak transmissions have been normalized to unity but do not reflect differences in total system (telescope + camera + filter) throughputs (for comparisons see Larsson et al. 2013).

An archival *IUE* spectrum of the M31 bulge near the location of SNR 1885 (Burstein et al. 1988) is shown in the lower panel of Figure 1 along with the *HST*/FOS spectrum of SNR 1885 (Fesen et al. 1999). The upper line is the bulge spectrum, while the lower line is the spectrum absorbed through SNR 1885, expected in the case of *IUE*, observed in the case of FOS. M31's bulge's UV flux is relatively weak and drops significantly shortward of 2900 Å but then slowly declines out to 2400 Å.

2.1. Previous SNR 1885 and M31 Bulge Images

Prior ACS/WFC and ACS/HRC images taken of SNR 1885 have been presented and discussed by Fesen et al. (2007). These images included Ca I (FR423N) and Ca II (FR388N) images, along with 4600 Å and UV continuum images taken with filters FR462N and F330W, respectively, to allow background subtraction for the Ca I and Ca II images.

These images also included a 15,600 s ACS/HRC exposure with the F250W filter, which resulted in a weak detection of the remnant in absorption. This filter encompasses the strong Fe II 2585, 2599 Å resonance lines but also covers the Mg II $\lambda\lambda$2796, 2803 Å doublet and Mg I 2852 Å leaving ambiguity as to how much of the observed absorption should be attributed to Fe II or to Mg I and Mg II. The new WFC3 Fe II image reported in the present paper uses a shorter wavelength filter, namely F225W, to avoid contaminated from these lighter elements.

Because M31 has been a target for several *HST* imaging programs, additional images in the *HST* archive were examined. These included 2010 and 2011 images taken as part of an emission line survey of the M31 nucleus encompassing the SNR 1885 site obtained with WFPC3/UVIS (GO:12174, PI: Z. Li). This survey comprised a set of 2700 s exposures in Hα (F656N), Hα off-band F665N), [N II] (F658N), [O III] (F502N), V band (F547M), Ca II H and K (F390M), and [O II] (F373N). The Ca II F390M passband has a FWHM $\approx$ 200 Å centered at 3900 Å, about twice the width of the Ca II FR388N ramp filter which was centered at 3950 Å (see Fesen et al. 2007). No Hα or [O III] emissions were detected at the location of SNR 1885 in the M31 survey image data (see Section 3.1) but absorption was detected in the Ca II filter F390M, and also in the nominal [O II] $\lambda\lambda$3726, 3729 filter (F373N), which can be attributed to Fe I 3720 Å absorption (see below).

2.2. Fe I Image Data

Four different filter images detected Fe I line absorption from SNR 1885. An ACS/WFC Fe I 3720 Å absorption image was obtained during five orbits on 2009 December 14 using the narrow passband [O II] ramp filter FR388N. The total exposure time was 12,700 s, comprising 11 separate images dithered by a four-point square dither pattern.

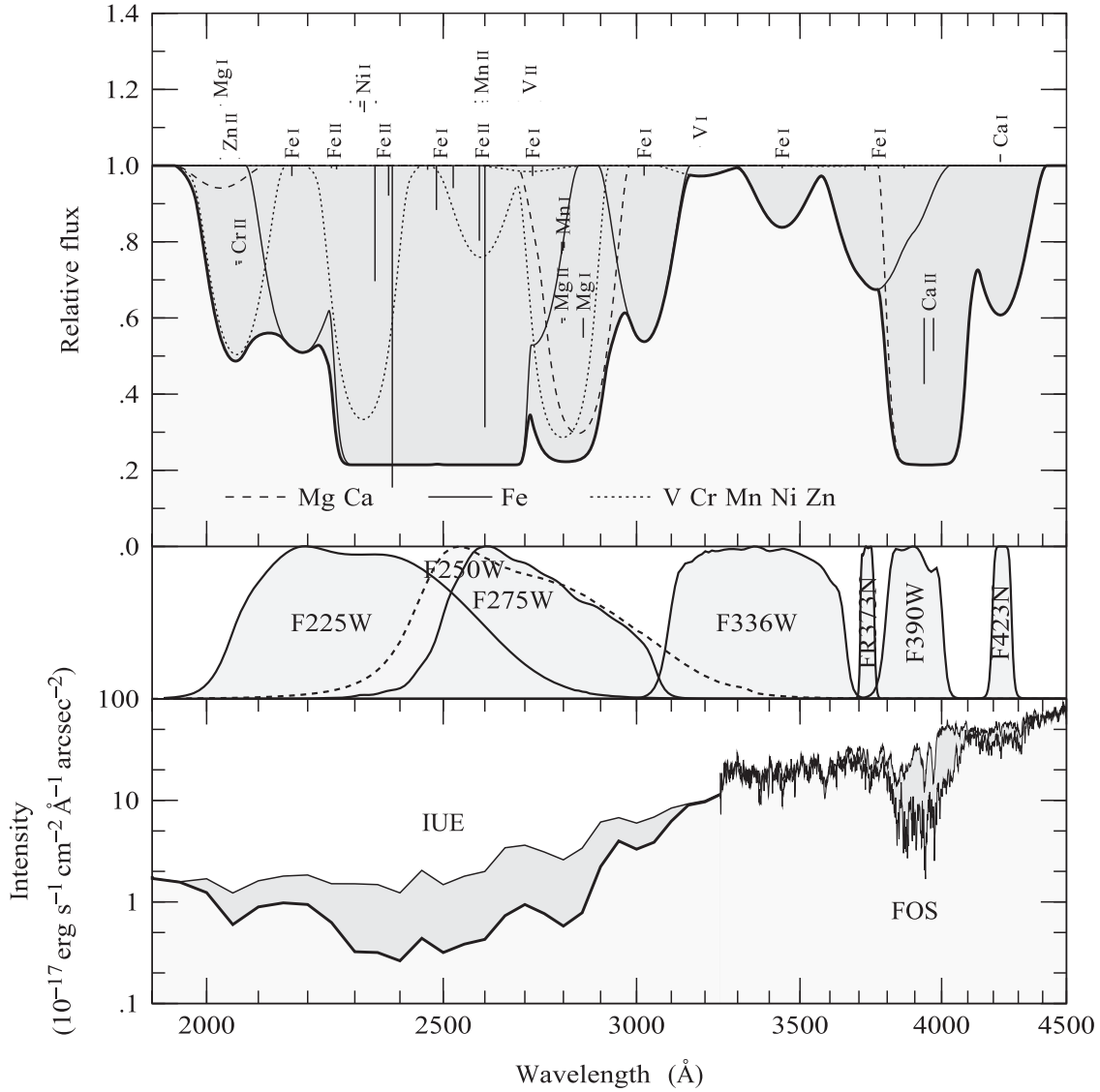

Figure 1. Top: model UV-optical absorption spectrum of SN 1885, from Fesen et al. (1999) vertical lines, with lengths proportional to oscillator strengths, mark wavelengths of the strongest lines. Middle: bandpasses for the WFC3 F225W, F275W, F336W, and F390M filters, along with the ACS/HRC F250W and ramp FR388N filters, are shown with filter peak transmissions normalized to unity. See text for details. Bottom: archival *IUE* spectrum of the M31 bulge near the location of SNR 1885 (Burstein et al. 1988), along with the *HST*/FOS spectrum of SNR 1885 (Fesen et al. 1999). The upper line is the bulge spectrum, while the lower line is the spectrum absorbed through SNR 1885, expected in the case of *IUE*, observed in the case of FOS.

The ramp filter was positioned so as to yield a peak transmission at the SNR 1885 site of 45% for line center of the Fe I line at 3720 Å. The filter's narrow passband (FWHM ≈ 70 Å; Figure 1) limits detection of Fe I 3720 Å absorption mainly to expansion velocities of ±3000 km s^{-1}, although the full 100 Å bandpass is sensitive to velocities as high as ±5000 km s^{-1}. Because the filter's transmission was only 2% at 3763 Å, it effectively blocked contamination from high-velocity Ca II 3934 Å absorption (i.e., 3934 Å blueshifted by 13,000 km s^{-1} is 3763 Å).

A similar image showing Fe I absorption from SNR 1885 was obtained in 2010 December using the WFC3/UVIS filter F373N and taken as part of an emission line survey of the bulge of M31. The exposure time was 2700 s. The WFC3 F373N filter has a narrower bandpass (FWHM ≈ 50 Å) compared to the ACS/WFC FR388N filter and a redder centroid of 3730 Å. This means that the WFC3 F373N image is sensitive to a slightly different range of Fe I 3720 Å velocities relative to the ACS FR388N image, but still uncontaminated by Ca II 3934 Å absorption.

Two broad passband ACS/HRC and WFC3/UVIS filter images also detected the remnant's Fe I absorptions. An ACS/HRC F330W image with a total exposure time of 5200 s was taken in 2004 October, and a three WFC3 F336W filter images totaling 5220 s were obtained in 2010 July. These ACS/HRC F330W and WFC3/UVIS F336W filters mainly provide information on an adjacent wavelength region relatively free of strong absorption features and thus are are primarily sensitive to the remnant's stellar background. However, both filters cover the Fe I line at 3441 Å and thus both show Fe I absorption from SNR 1885. These images are also weakly sensitive to blueshifted Fe I 3021 Å absorption. While these camera + filters combinations have similar bandpasses, the integrated system throughput for the WFC3/UVIS F336W is nearly twice that of the ACS/HRC F330W resulting in a higher S/N.

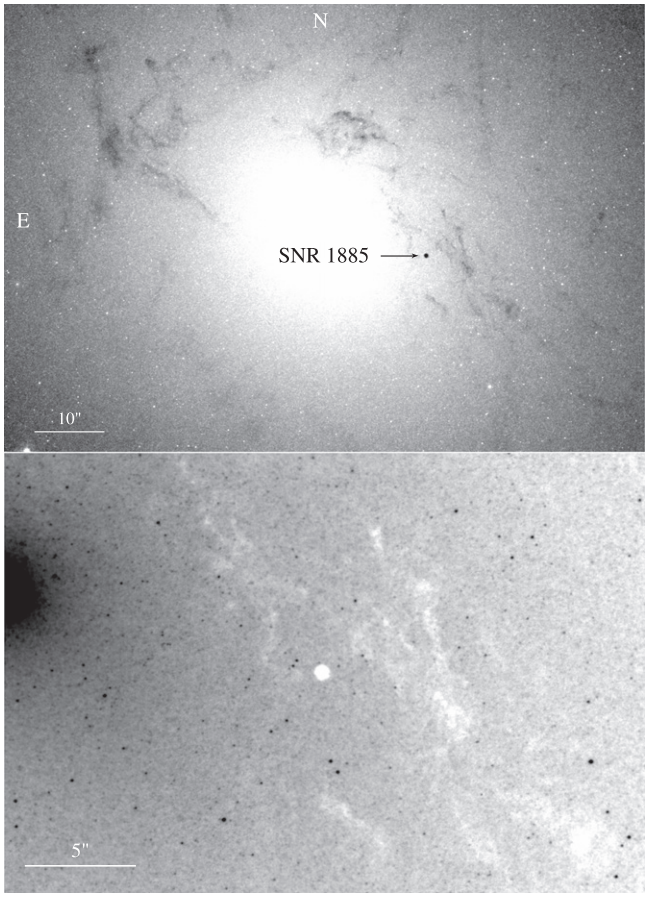

Figure 2. 2010 December WFC3 image of the bulge of M31 taken with the F390M filter as part of an emission line mapping program of the nuclear regions of M31 (PI: Z. Li). A positive linear stretch of the M31 bulge is shown in the upper panel. The remnant of SN 1885 (S And) appears as a small (0.″8) round dark spot of Ca II H and K absorption 16″ southwest of the nucleus. The bottom panel shows an enlarged section of this same image centered on the SN 1885 region but shown in a negative log stretch.

2.3. Fe II Image Data

Imaging the remnant's Fe II required using filters sensitive to the wavelength region between 2300 and 2600 Å. Bandpasses for the WFC3 F225W, F275W, and F336W filters are shown as shaded regions in Figure 1.

The WFC3/UVIS F225W filter is the best for detecting SNR 1885's Fe II absorption free from contamination from other sources. It has a FWHM ≈ 500 Å bandpass with a peak transmission of 8.6% centered around 2300 Å, as illustrated in Figure 1. The principal expected absorbers in this band are the strong UV resonance lines of Fe II at 2343, 2382 Å, with small contributions from Fe I 2483, 2523 Å and Ni I around 2300 Å. The filter also catches the strong Fe II lines at 2586, 2599 Å in its red wing.

Thus this filter's bandpass provides detection dominated by Fe II and largely free of contamination by lighter elements. In contrast, both the WFC3 F275W and the ACS/HRC F250W filter have bandpasses sensitive to Mg I and Mg II in addition to Fe II (Figure 1).

A series of WFC3 F225W images of SNR 1885 were obtained during nine orbits split into three visits that occurred on November 17 and 21 and 2012 December 1. The resolution of the WFC3 camera is 0.″039 per pixel giving it a slightly better angular resolution scale than the 0.″049 of the ACS/WFC Fe I image and previous WFPC2 images of Ca I and Ca II (Fesen et al. 1999).

Twelve individual images were taken during each of the three visits, dithered with a primary three-point and secondary four-point pattern. There was a small error in guiding for the third set of images (ibr803030) which resulted in a slightly smeared image in one direction. The images from the three visits were co-aligned with IRAF tasks and stacked into one final 3 × 8064 s = 24,192 s exposure.

One additional orbit was used to obtain an off-band image of the remnant and M31 bulge. The off-band image used the WFC3 F336W filter which has a FWHM ≈ 550 Å bandpass with a peak transmission of 19% around 3300 Å, as illustrated in Figure 1. The total exposure of this dithered image was 2724 s. Archival WFC3 F336W images of were also examined.

3. RESULTS

Ideally one would like images of SNR 1885 to be spatially well-resolved and of high S/N. However, the small size (0.″8 diameter) and faintness of the bulge of M31 in the UV make such images challenging to secure. Moreover, interpretation can be ambiguous in wavelength bands where absorptions from multiple species and ionization states overlap.

From this perspective, the cleanest images are the high resolution Ca II FR338N image reported by Fesen et al. (2007) and the Fe I and Fe II images presented here. Both Ca II and Fe II are expected to be the dominant ion of their element—the singly ionized ion—and both species are expected to dominate absorption in the respective filters. As will be discussed below, the Ca II, Fe I, and Fe II images reveal distinctively different structures.

3.1. Ca II in SNR 1885

Figure 2 shows a 2700 s *HST* WFC3 F390M filter image of the central region of M31. SNR 1885 is the small circular spot (dark in the upper panel and white in the lower panel) approximately 10″ west and 4″ south of the M31's nucleus. Taken using the 200 Å wide F390M filter, the presence of SNR 1885 is striking against M31's bulge light and places the remnant in context within the galaxy's nuclear region.

The remnant is visible in Ca II H and K line absorptions from the remnant's Ca-rich ejecta. Images such as this illustrate how prominently the remnant of SN 1885 can appear in absorption.

SN 1885 fortunately exploded on the near side of the bulge, so that its expanding remnant is well back-lit by M31 bulge stars. It is also a fortuitous that the remnant's projected location lies some distance away from several M31 bulge dust lanes (see Figure 2) thus making analysis of the remnant's absorption less confused.

Although seen prominently in filter images sensitive to strong resonance lines, such as Ca II, SNR 1885 is virtually invisible at nearby continuum wavelengths. Figure 3, reproduced from Fesen et al. (2007), demonstrates how SNR 1885 can be so clearly detected in filter images that are sensitive to strong resonance lines, such as in this case the Ca II 3934, 3968 Å H and K lines, whereas it is virtually invisible at neighboring wavelengths, in this case 4600 Å using the F462N filter which lacks any significant resonance line features. The lack of any hint of the remnant in the 4600 Å image also indicates that SN 1885 generated virtually no appreciable dust. This situation along with the lack of any detectable Hα or [O III]

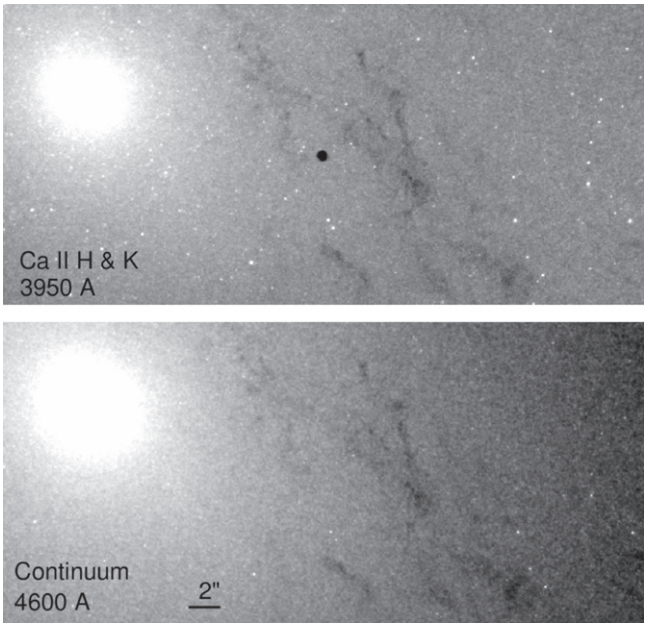

Figure 3. Top: ACS/WFC FR388N image of the M31 bulge shows SNR 1885 prominently visible via Ca II 3934,3968 Å K & H absorption. Bottom: ACS/WFC F462N continuum filter image of the same region showing no hint of the remnant.

line emissions associated with the remnant (see Figure 4) helps explain the lack of any optical detection of SNR 1885 before its discovery by Fesen et al. (1989) despite several searches.

3.2. *Fe I in SNR 1885*

Figure 5 shows four *HST* ACS and WFC3 images of SNR 1885 which are sensitive to the remnant's near-UV Fe I absorption lines. In order to make clear the location of the remnant, a 0.″7 diameter circle is shown on these images to mark the extent of the remnant's prominent Ca II H and K absorption.

The upper left panel shows an ACS/WFC Fe I 3720 Å absorption image. A similar image is shown in the upper right hand panel which shows a F373N exposure obtained with WFC3/UVIS. The Fe I absorption is seen extended in both images with a diameter of ≈0.″4 and displaced eastward from the remnant's center as defined by Ca II images.

While these images are fairly similar in appearance, there are slight differences. The peak of Fe I absorption is displaced eastward 0.″11 ± 0.″03 from remnant center in the FR388N image but slightly less so (0.″08 ± 0.″03) in the F373N image. Such a difference is only marginally significant given the S/N of the data but, if real, may simply be due to differences in the two filter bandpass widths and centers. Filter bandpass differences probably also account for differences seen in the

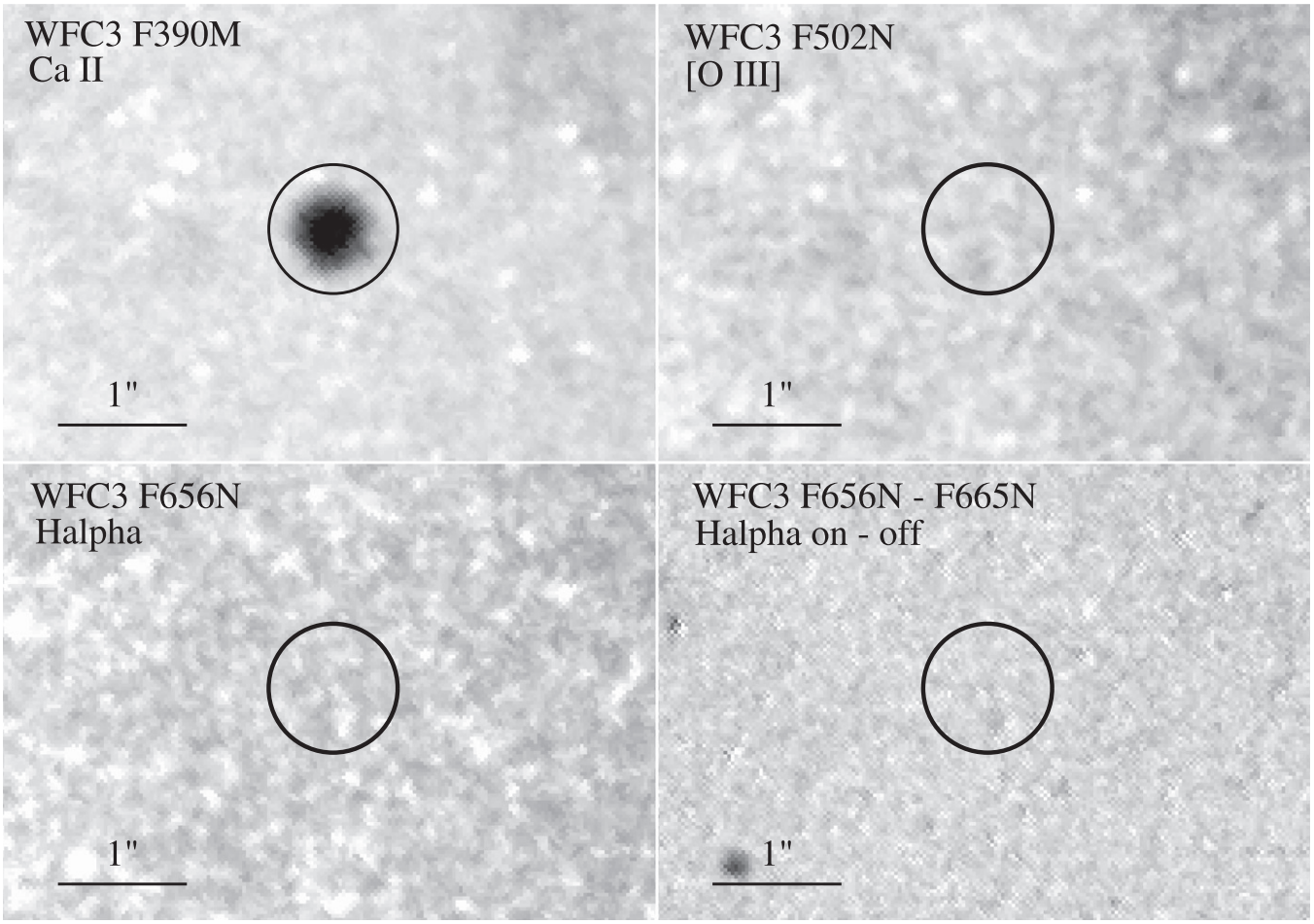

Figure 4. [O III] and Hα images of the site of SN 1885. Upper left image shows SNR 1885's Ca II absorption as a reference. Lower right image is a difference image constructed from Hα "on" and "off" F656N and F665N images. Circles are 1 arcsec in diameter.

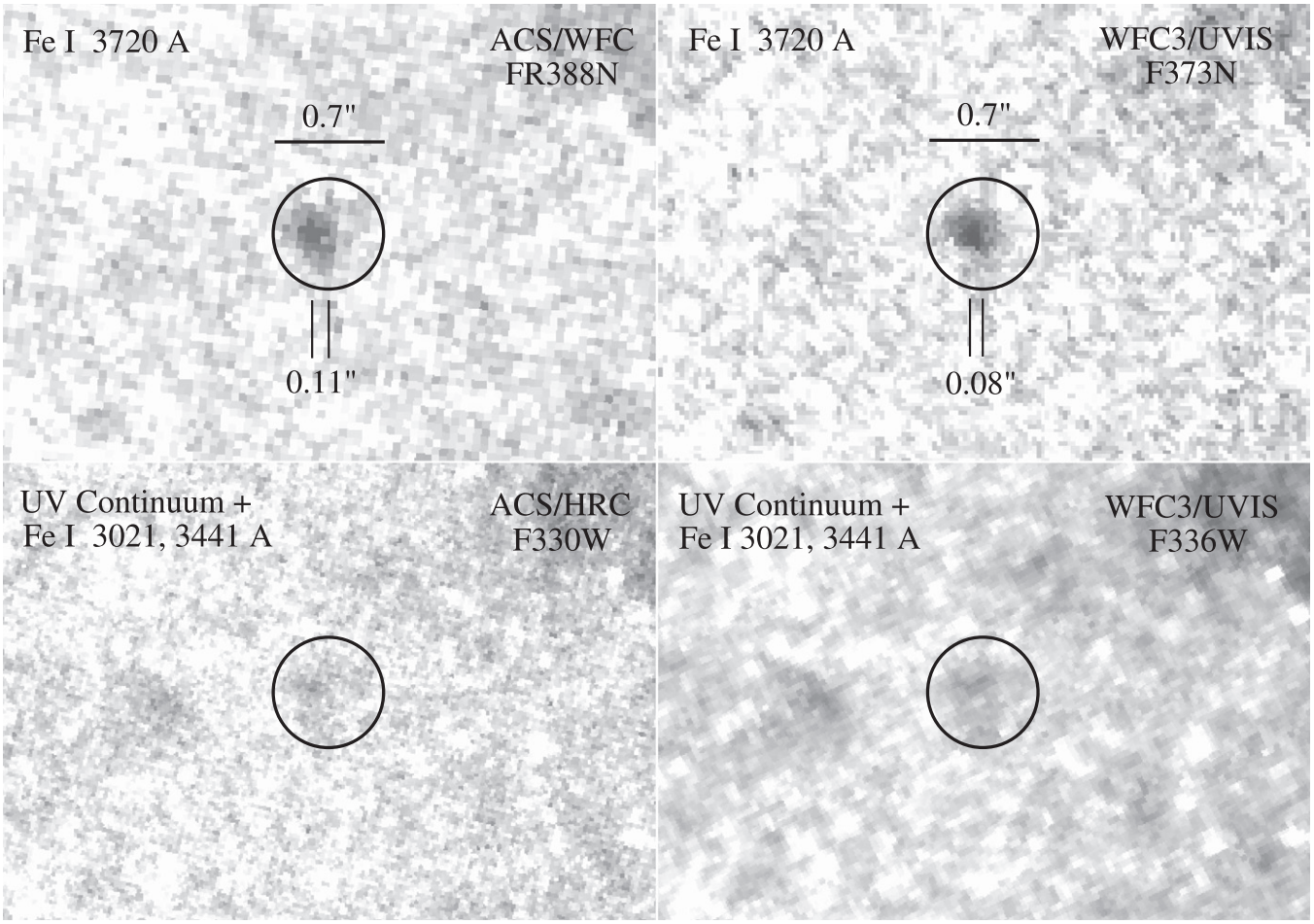

Figure 5. Top row: ACS/WFC FR388N and WFC3/UVIS F373N images of SNR 1885, sensitive to Fe I 3720 Å absorption. Bottom row: ACS/HRC F330W and WFC3/UVIS 336 W images sensitive to Fe I resonance lines at 3020 and 3441 Å, and should be relatively uncontaminated by absorption from lighter elements. The 0.″7 diameter circle on each panel marks the extent of strong Ca II absorption. North is up and east to the left for all images.

darkest (most absorbed) regions of SNR 1885 due to Fe I 3720 Å; 0.60 ± 0.05 and 0.40 ± 0.07 times the bulge background flux for the FR388N and F373N images, respectively.

More importantly, both images show an Fe I absorption patch that is distinctly smaller than that of either Ca II or Ca I (Fesen et al. 2007). Also, unlike the remnant's Ca II or Ca I absorptions, the detected Fe I absorption gives no sign of being confined to a shell.

Broader passband ACS/HRC F330W and WFC3/UVIS F336W images of the remnant are shown in the lower two panels of Figure 5. Both images show weak absorption within the remnant (as marked by the circle indicating the extent of strong Ca II absorption) due mainly to Fe I 3441 Å absorption. The amount of light bulge light blocked by SN 1885 in the ACS F330W and WFC3 F336W images potentially due to both Fe I 3021 and 3441 Å line absorptions within the 0.″7 circles shown in Figure 4 is only $\simeq$5%, indicating that these images are mainly continuum images.

These images again show an eastward displacement of the peak Fe I absorption. However, unlike the Fe I images taken with narrow passband filters seen in the upper panels, these images reveal a larger patch of Fe I absorption, extending farther to the south and west, with the absorption appearing less concentrated than in the narrow filter images. The full area of Fe I absorption is best seen in the WFC3 F336W image which has higher S/N due to greater camera + filter throughput.

While the observed off-center displacement of Fe I mass could suggest a velocity asymmetry around 3500 km s^{-1}, similar to the maximum values obtained for SNe Ia from late-time, near-IR spectra (Maeda et al. 2010), there is reason to doubt this explanation given the similar eastern offset of the remnant's Ca I (Fesen et al. 2007). Fe I, like Ca I, has a relatively short lifetime in SNR 1885, only about 10 yr due to photoionization by UV light from the bulge of M31.

The persistence of Fe I and Ca I some 130 yr after explosion suggests that these ions may be self-shielded by their own continuum optical depth (Hamilton et al. 1991; Fesen et al. 2007). The current presence of Fe I and Ca I concentrated along the eastern half of the remnant and unexpectedly *toward* the M31 nucleus, suggests an important source of ionizing UV photons along the remnant's projected western hemisphere. If this is the case, the remnant's Fe- and Ca-rich ejecta in its western half could have self-shielded ejecta in the remnant's central and eastern regions leading to the different Ca I/Ca II and Fe I/Fe II absorption distributions observed. Since Fe I likely represents only a small percentage of the remnant's Fe-rich ejecta mass, Fe I images may not accurately portray the true distribution of SNR 1885's Fe-rich material.

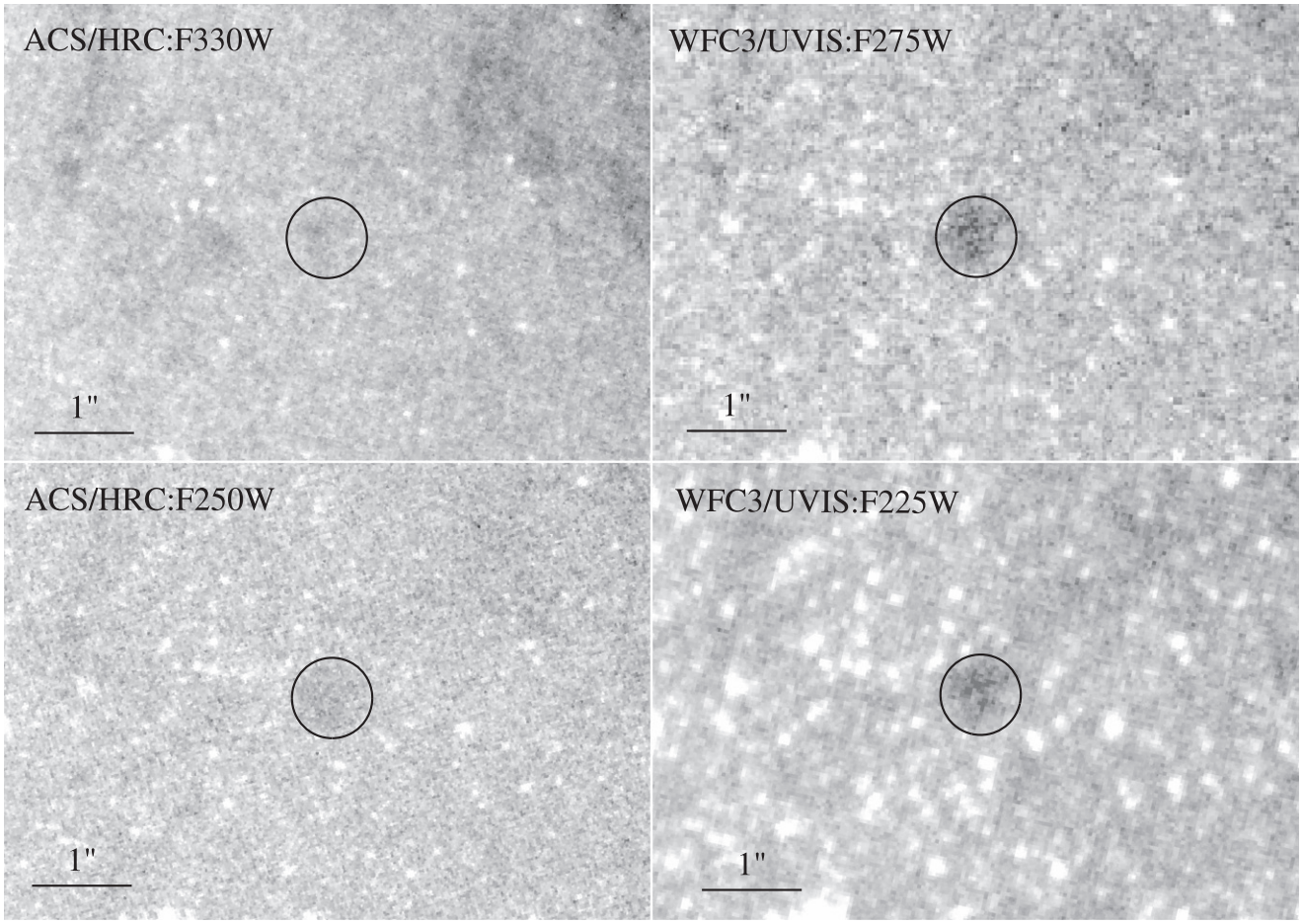

Figure 6. Near UV images of SNR 1885. showing the remnant's detection. Upper panels: ACS/HRC F330W filter image (left) sensitive to Fe I and 3100–3700 Å continuum, and a WFC3 F275W filter image (right) sensitive to 2500–3050 Å flux. Lower panels: an ACS/HRC F250W image (left) sensitive to 2400–3200 Å flux, and a WFC3 F225W filter image (right) sensitive to 2100–2700 Å flux.

3.3. Fe II in SNR 1885

The three *HST* images taken of SNR 1885 which cover the near-UV wavelengths of strong Fe II resonance lines (Morton 1991) are shown in Figure 6. This Figure also includes the broad passband ACS/HRC F330W discussed above in regard to the remnant's Fe I absorption and is included here to show the stellar background and dust lanes at and around the SNR 1885 site. All four images are shown using a square root intensity stretch in order to show both the remnant's absorption features and neighboring bulge features.

These images show numerous bright bulge stars in the vicinity of SNR 1885 which are probably mainly red giants with strong UV coronal line emissions. Individual bulge stars become increasingly prominent at shorter wavelengths and are most apparent in the F225W filter image seen in the lower right panel. The F330W image, with a passband comparatively free of line absorptions suggests that with the exception of two stars along the remnant's westernmost limb, no bright foreground or background stars lie in the direction to SNR 1885.

Although the F225W, F250W, and F275W filter passbands cover some or all of the strong Fe II lines at 2343, 2382, 2586 and 2599 Å, the detected absorption in SNR 1885 appears different in each filter. Below, we discuss possible reasons for these differences.

We begin with the ACS/HRC F250W filter image which has been presented and discussed by Fesen et al. (2007). This image yielded the weakest detection of the remnant. Given the HRC's small pixels and only a 6% integrated system throughput for the ACS/HRC + F250W filter, the resulting low S/N image showed a featureless absorption spot but one whose diameter is nearly the same as that of the remnant's Ca II absorption. The F250W filter has a relatively broad passband which is starts at 2300 Å peaks at 2500 Å and extends to 3300 Å. This makes this filter sensitive to several strong resonance lines including Fe I, Fe II, Mg I, and Mg II. Thus, this image is likely a composite of Fe and Mg absorption features, limiting its usefulness for determining the remnant's Fe II 2D distribution.

The WFC3 F275W image is fairly similar to the F250W image but with hints of some internal structure. Like that of the F250W filter, F275W's bandpass encompassed many likely absorption lines including Fe I, Fe II, Mg I, and Mg II.

The most plausible explanation of differences between the F250W and F275W images is that the F275W image is picking up substantial more absorption from resonance lines of Mg II 2796, 2804 Å and Mg I 2853 Å due to the WFC3's higher throughput at 2800 Å. Note that the model spectrum shown in the top panel of Figure 1 is for a line of sight directly through the center of SNR 1885. If SNR 1885 has Fe concentrated to

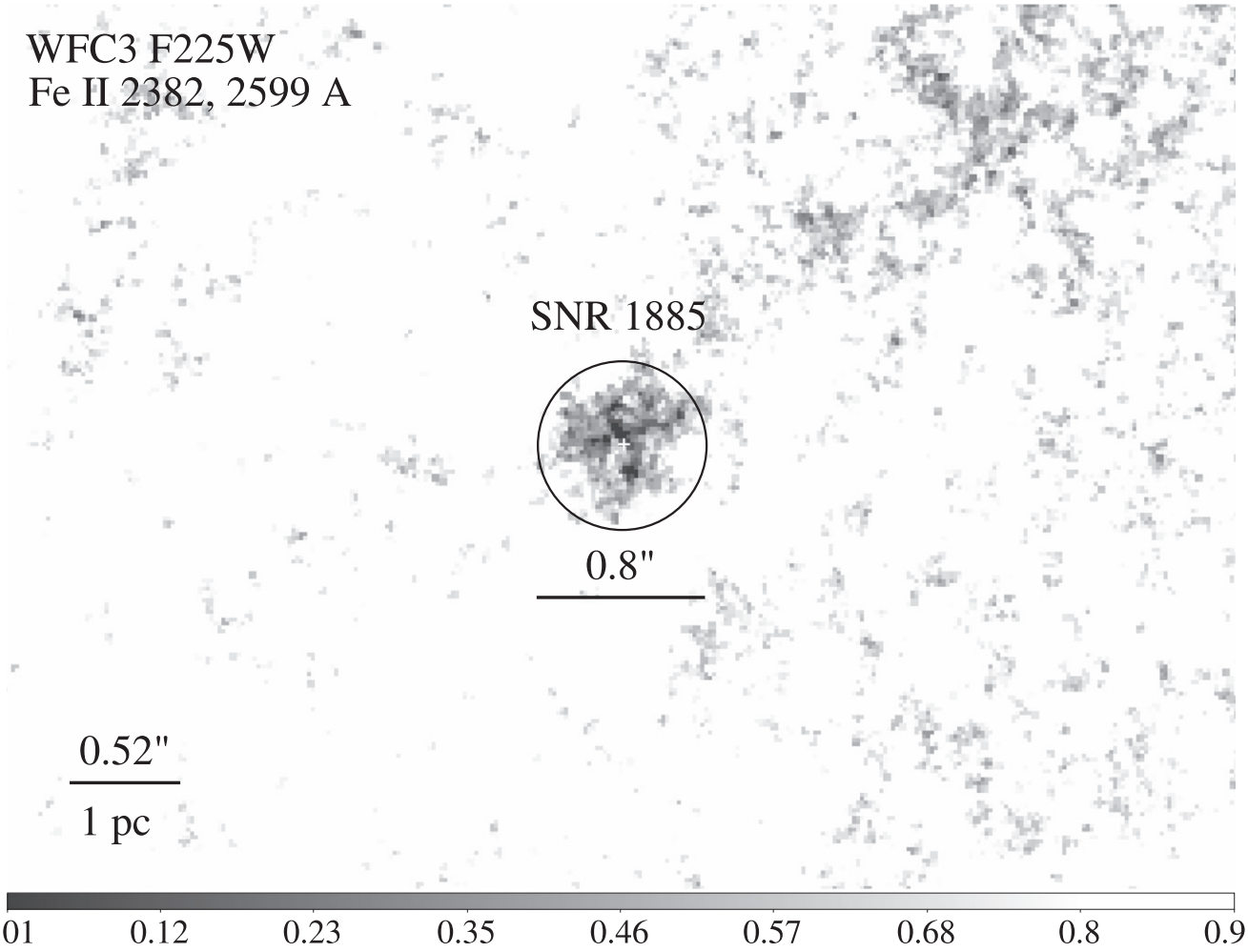

Figure 7. WFPC3 F225W Fe II image of SNR 1885 shown in a high contrast, linear intensity stretch. The circle (radius of 0.″4) and its center (white cross) indicates the maximum extent and center of the remnant's detected Ca II H and K line absorption. Expansion of 0.″4 over a 125 yr time span corresponds to an average expansion velocity ≃12,000 km s^{-1} at M31's 785 kpc distance.

the center and lighter elements concentrated in a shell, then a line of sight through the outer parts of SNR 1885 would show relatively more absorption from Mg and less from Fe.

The F225W WFC3 image (lower right panel in Figure 6) provides the cleanest image of Fe II absorption in SNR 1885, uncontaminated by Mg absorption features. As illustrated in Figure 1, the strongest absorption lines in the WFC3 F275W filter are Fe II 2586, 2599 Å, while the strongest lines in the WFC3 F225W filter are Fe II 2343, 2382 Å. Since the strongest lines in both filters are those of Fe II, we had expected that the two images would show essentially the same structure. But this is not so: the F275W image shows absorption that is smoother, more extended, and less centrally concentrated than F225W likely due to added Mg I and Mg II absorption.

The WFC3 F225W Fe II image shows a structure that differs strikingly from that of either Ca or Fe I. It reveals four prominent Fe II absorption streams or plumes that extend from the center of the remnant to near the outer extent of the Ca II absorption.

Figure 7 shows an enlargement of the Fe II F225W image. The four apparent Fe II streams appear clumpy, have similar thicknesses (∼0.″1), and intersect at a point ≃0.″05 (≃1500 km s^{-1}) north of the center of the remnant as defined by the remnant's Ca II absorption. While the detected Fe II absorption is strongest in these four plumes, there is also considerable absorption outside these finger-like plumes extending out to a radius ≃0.″3 (≃10,000 km s^{-1}).

A major concern in interpreting the F225W Fe II image is uncertainty regarding the distribution of background stellar sources as they could affect the distribution of observed light and dark (absorption) features. After all, the M31 bulge around SNR 1885 exhibits a high density of strong stellar sources in the F225W image. For example, a few bright UV stars located in front of or behind the remnant could potentially lead to an uneven absorption structure not unlike that seen in the F225W image.

Although we cannot rule out this possibility, we view this as unlikely. From the predicted UV spectrum of SNR 1885 shown in Figure 1, it is not possible to have a clean "off-band" Fe II image around 2500 Å from which one could determine the number and brightness of background stars toward SNR 1885. However, as noted above, the ACS/HRC F330W image indicates no bright line-of-sight stellar contamination, especially toward the remnant's center.

Moreover, while the density of stars in the F225W image surrounding SNR 1885 is fairly high (∼5–8 stars arcsec^{-1}, there are several immediately adjacent bulge regions just to the west ∼1″ in diameter largely free of bright stars. Further, the nearly

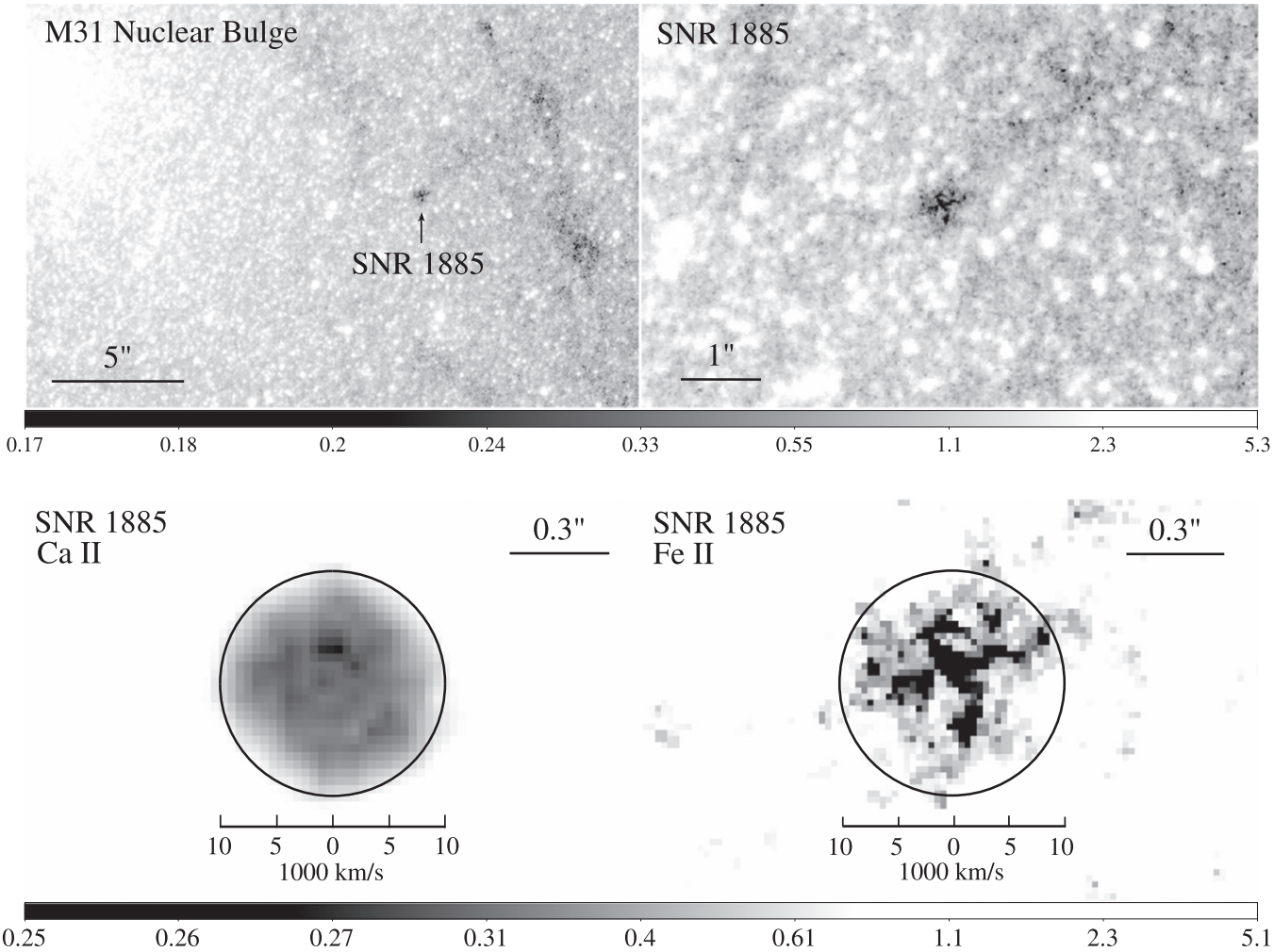

Figure 8. Upper panels: wide and narrow WFC3 F225W views of M31's western bulge region showing SNR 1885 in context with neighboring dust lanes. Lower panels: log intensity stretched views of SNR 1885 as seen in Ca II and Fe II images. The circles shown (radius = 0.″342) correspond to an average expansion velocity of 10,000 km s^{-1} since 1885. Note the presence of clumpy, interior Ca II absorption and the extent of Fe II absorption "plumes" out past these Ca II absorption clumps reaching in places to the edge of the Ca II absorption. The intensity bar refers to both the Ca II image and Fe II images.

orthogonal plume structure observed in the F225W image is unlikely to be due to a chance distribution of background stars. If the similar thickness Fe II plumes intersecting near at the remnant's center and occupying only the inner two-thirds of the remnant's radius was caused by a chance arrangement of bright background stars, then their presence would be expected to have a significant impact on the otherwise smooth and largely spherical Fe II absorption detected in between the plumes.

In addition, nothing so striking in morphology as seen in the F225W image is visible in any neighboring M31 bulge dust lanes. This is shown in the upper panels of Figure 8 where we present a wider and log intensity stretched view of the F225W image. The depth of the apparent Fe II absorption in SNR 1885 seen in the F225W image is equal to or greater than that seen in neighboring M31 bulge dust lanes.

The darkest (most absorbed) regions in the F225W image of SNR 1885 are less than 0.15 times the diffuse (no stars) bulge background flux, with the remnant's inner 0.″4 diameter region encompassing all four plumes is $\leqslant$50% below that of the least bright adjacent bulge regions. The total measured flux in the F225W filter for SNR 1885 within a circular region shown in Figure 8 ($r = 0.''34$) is $0.60^{+0.50}_{-0.15}$ that of neighboring bulge regions at similar distances from the M31 nucleus.

The four Fe II plumes exhibit different projected lengths, with the one to the west extending the farthest, nearly out to the edge of the remnant's strong Ca II absorption shell (0.″34; see Figure 8) implying a maximum transverse velocity $\simeq$10,000 km s^{-1}. If these Fe II plumes truly trace the distribution of the remnant's Fe-rich ejecta, the different lengths could arise from line of sight projections of nearly equal length plumes but expanding in different directions.

SNR 1885's 2D Fe II absorption stands in stark contrast to its Ca II absorption distribution, also shown in Figure 8 for easy comparison. Whereas the remnant's Ca II is concentrated in a clumpy shell spanning a range 1000–5000 km s^{-1} in expansion velocity, the remnant's Fe-rich ejecta is concentrated in the four finger-like plumes which extend well past the Ca-rich shell. Of equal importance is the apparent presence of Fe-rich material out to $\approx$10,000 km s^{-1} in transverse velocity in non-plume directions.

The significance of the apparent $\simeq$1500 km s^{-1} (0.″05) off-center intersection of the Fe II absorption fingers relative to the remnant's Ca II absorption is difficult to assess given indications that the remnant's Ca II absorption is not perfectly symmetric. The maximum Ca II absorption seen in both ACS FR388N and WFC3 F390W images exhibits a slight extension (~0.″07 off the southwestern limb; see Figure 5 in

Fesen et al. 2007). Moreover, the remnant's 0.″80 Ca II diameter seen in the most recent 2010 images indicates a somewhat smaller $11{,}900 \pm 1500\,\mathrm{km\,s^{-1}}$ transverse velocity than the $12{,}400\,\mathrm{km\,s^{-1}}$ estimated by Fesen et al. (2007) and lower but still within the uncertainty of the $13{,}100 \pm 1500\,\mathrm{km\,s^{-1}}$ radial velocity measured from the remnant's Ca II H and K absorption profile (Fesen et al. 1999). Small radial and transverse velocity differences might indicate a slight non-spherical expansion, meaning an apparent off-center displacement of the Fe II absorption may not be significant and not a clue for an off-center ignition point of SN 1885.

4. DISCUSSION

We will now discuss how the new *HST* observations of the remnant of S And (SNR 1885) can be placed in context of our current understanding of SNe Ia. The most informative *HST* images of SNR 1885 presented above are those in Ca II absorption and Fe II absorption (Figure 8). This is because both Ca II and Fe II are expected to be the dominant ion of that element so their absorption reliably traces the element as a whole, and because the absorption in the chosen filters, FR338N and F225W, respectively, is dominated by the designated ion, relatively uncontaminated by absorption from other species.

The presence of Fe at the center of SNR 1885 with Ca-rich debris in a shell around the center is consistent with SN 1885 being a Type Ia supernova, albeit likely a subluminous SN Ia. Because its debris are still in near free expansion after 130 yr, it retains the density distribution established shortly after the explosion. Thus, the distribution of elements in SNR 1885 can provide valuable kinematic information about the general properties and character of a Type Ia explosion.

Consistent with evidence from SNe Ia light curves, the remnant of SN 1885 shows evidence for both deflagration and detonation. A characteristic signature of detonations is an approximately spherically symmetric layered structure of burned elements. Hence, the shell-like appearance of Ca II, an incompletely burned element, points to a detonation explosion. *HST* images show a layered structure for the intermediate mass elements such as Ca in SNR 1885 (Fesen et al. 2007); specifically, the presence of inner clumps of Ca at velocities between 1,000 and $5{,}000\,\mathrm{km\,s^{-1}}$ along with Ca debris with expansion velocity out to $\simeq 12{,}500\,\mathrm{km\,s^{-1}}$ and thus is strongly suggestive of a detonation phase.

In contrast, the Fe II F225W image of SNR 1885 shows several finger-like plumes that extend from the center out to an expansion velocity of about $10{,}000\,\mathrm{km\,s^{-1}}$, near the outer edge of the Ca II absorption. The length scale of the lumps seen in SNR 1885 is consistent with Rayleigh–Taylor instabilities commonly found in SNe Ia simulations during the early deflagration phase. Though the Fe II image shows just four plumes, this may be a projection effect when combining a small number of plumes. In summary, the combined Ca and Fe distributions in the remnant of SN 1885 is in line with an off-center delayed detonation SN Ia event.

For SNe Ia, several explosion scenarios are possible including classical delayed detonation, pulsating delayed-detonation models (Khokhlov 1991; Yamaoka et al. 1992; Khokhlov et al. 1993; Höflich et al. 1995; Gamezo et al. 2005; Röpke et al. 2007), or dynamical merger models (Benz et al. 1990; Rasio & Shapiro 1994; Isern et al. 2011; Pakmor et al. 2011). For the newly recognized subclass, SNe Iax (Li et al. 2003, 2011; Foley et al. 2013), models suggested include deflagration models with burning of the outer layers of a WD (Kromer et al. 2013) or pulsating delayed detonation models (Stritzinger et al. 2014).

However, the seeming lack of appreciable Ca-rich material in the center argues against strong mixing and in favor of the explosion of a massive WDs. The fact of limited mixing of the inner region and the constraint of plumes to the low velocities seen compared to the mixing predicted by hydro-models (Reinecke et al. 2002; Gamezo et al. 2003; Röpke et al. 2007; Seitenzahl et al. 2013) suggest some suppression of the Rayleigh–Taylor instability possibly through strong magnetic fields (Höflich et al. 2004, 2013; Penney & Höflich 2014; Reming & Khokhlov 2014).

We split the following discussion into in the constraints for M_{Ch} mass models or, more precisely, the constraints for the deflagration phase of burning, arising from dynamical WD mergers and in the framework of SNe Iax. The approximately spherically symmetric distribution of Ca II in contrast to Fe II plumes which extend in different directions argues against an explosion with a preferred symmetry axis as might result from an anisotropic merger of two white dwarfs.

Within the framework of merging WDs, the large angular momentum will impose a preferred axis of symmetry which should be apparent in our 2D images but is clearly not the case. A detonation front is responsible for burning without time for the formation of chemical clumps and mixing. Thus, none of the dynamical models show large scale, irregular structures if the merging occurs on time scales of the orbiting WDs.

One exception are the type of violent, dynamical mergers in which two WDs collide. Simulations show that some of the Fe-rich material is squeezed out into a thin, "cone-like" structure which can extend to high velocities. Instabilities by the decay of radioactive ^{56}Ni over the time may produce clumps in the thin structure. However, we see several structures without a regular pattern and thus the distribution of the intermediate element of Ca in SNR 1885 seems to be inconsistent with this model.

Finally we consider SN Iax events which have been classified as a new type of thermonuclear explosions. Though the prototype SN 2002cx was several magnitudes dimmer than S And, the recent SN 2014 Z extended the range to −18 mag, similar to S And. What sets SNe Iax apart from normal SNe Ia is that the former does not show a brightness decline relation and spectra similar to SN 1991 T. Considering the uncertainties in the light curve of S And given its location against the bright M31 bulge background, SNe Iax may well be compatible.

The nature of SNe Iax is currently under debate and may include deflagration burning and ejection of the outer layers of a WD leading to a low density shell (Kromer et al. 2013) and/or pulsating delayed detonation models (Stritzinger et al. 2014). The low-ejecta mass of the first class is unlikely because it in conflict with the long time scale of re-ionization and the layered structure. However, pulsation delayed-detonation models can not be excluded because they can have a wide variety of mixing during the pulsation, and show a layered structure in the outer layers. An alternative interpretation to the structure may be various amounts of mixing during the or multiple pulsations of the WD.

5. CONCLUSIONS

The remnant of the probable Type Ia remnant of SN 1885 (S And) in the bulge of M31 is visible in absorption against the background of bulge stars. High resolution *HST* images of the remnant of SN 1885 in M31 show the following:

1. The distribution of Fe I material appears small (0.″3), and offset to the east by approximately 0.″1 from the remnant center. While this displacement might indicate a velocity asymmetry of the remnant's Fe-rich material like that proposed by Maeda et al. (2010) based on near-IR spectral observations of SNe Ia, a similar displacement of the remnant's Ca I absorption suggests it is due to an uneven ionizing UV flux local to the remnant.
2. A deep UV image sensitive mainly to Fe II resonance lines at 2343, 2382 Å shows an irregular shaped Fe II absorption structure peaked in strength at the center of the remnant with four plume-like extensions of especially strong Fe II absorption which weaken and terminate near the remnant's outer boundary as marked by the remnant's Ca II absorption extent.

The key result of this paper has been to present a spatially resolved *HST* image of the supernova remnant in absorption in the strong resonance doublet of Fe II and to compare that image to a previously obtained absorption image in Ca II H and K. Since Fe II and Ca II are expected to be the dominant ions of their respective elements, the images in these lines trace the bulk of iron and calcium in SNR 1885. Since the remnant is still in free expansion at the present time, some 130 yr after the explosion, the observed elemental distribution is the same as that established shortly after the explosion, thereby giving valuable insight to the explosion process.

Our finding that iron, the dominant outcome of nuclear burning to completion, shows four plumes that start at the center of the remnant and reach out to a maximum velocity of 10,000 km s^{-1}, near the maximum extent of Ca, is especially significant. Calcium, a partially burned element, is by contrast concentrated in a broad and lumpy shell spanning 1000–5000 km s^{-1} and extending out to a maximum of 12,500 km s^{-1}.

The observed distribution of iron and calcium in the remnant of S And is consistent with delayed detonation models of Type Ia explosions, in which the explosion begins as a deflagration at the center of a white dwarf, which later transitions to a detonation. The deflagration drives Rayleigh–Taylor unstable plumes to near the surface of the white dwarf. This deflagration burning heats and expands the white dwarf so that when the explosion turns into a detonation, unburned elements are burned not to completion but rather to intermediate mass elements, such as the calcium observed in the S And remnant.

Progenitors with $M_{\rm Ch}$ mass and, in particular, off-center delayed detonation models are favored by observations, including our previous studies of S And. However, such models have difficulty when taking into account the predicted burning instabilities and mixing during the deflagration phase, both with respect to the brightness decline relation, late-time IR spectra and, at least for subluminous SNe Ia, in early time and maximum light optical and IR spectra.

The structure observed in S And may serve as a benchmark to decipher the mechanism to partially suppress instabilities. Moreover, the evidence for the Rayleigh–Taylor instabilities suggested by the S And observations reported here support the validity of $M_{\rm Ch}$ models which require a deflagration phase and disfavor dynamical or violent mergers.

This research was supported by NASA through grants GO-10722 and GO-12609 from the Space Telescope Science Institute, which is operated by the Association of Universities for Research in Astronomy, and the NSF through grants AST-0708855 and AST-1008962 to PAH.

REFERENCES

Benz, W., Cameron, A. G. W., Press, W. H., & Bowers, R. L. 1990, ApJ, 348, 647
Bloom, J. S., Kasen, D., Shen, K. J., et al. 2012, ApJL, 744, L17
Branch, D., Livio, M., Yungelson, L. R., Boffi, F. R., & Baron, E. 1995, PASP, 107, 1019
Burstein, D., Bertola, F., Buson, L. M., Faber, S. M., & Lauer, T. R. 1988, ApJ, 328, 440
Chevalier, R. A., & Plait, P. C. 1988, ApJL, 331, L109
Colgate, S. A., & McKee, C. 1969, ApJ, 157, 623
de Vaucouleurs, G., & Corwin, H. G., Jr 1985, ApJ, 295, 287
Di Stefano, R., & Kilic, M. 2012, ApJ, 759, 56
Di Stefano, R., Voss, R., & Claeys, J. S. W. 2011, ApJL, 738, LL1
Fesen, R. A., Gerardy, C. L., McLin, K. M., & Hamilton, A. J. S. 1999, ApJ, 514, 195
Fesen, R. A., Höflich, P. A., Hamilton, A. J. S., et al. 2007, ApJ, 658, 396
Fesen, R. A., Saken, J. M., & Hamilton, A. J. S. 1989, ApJL, 341, L55
Foley, R. J., Challis, P., Chornock, R., et al. 2013, ApJ, 767, 57
Gamezo, V. N., Khokhlov, A. M., & Oran, E. S. 2004, PhRvL, 92, 211102
Gamezo, V. N., Khokhlov, A. M., & Oran, E. S. 2005, ApJ, 623, 337
Gamezo, V. N., Khokhlov, A. M., Oran, E. S., Chtchelkanova, A. Y., & Rosenberg, R. O. 2003, Sci, 299, 77
Garcia-Senz, D., & Woosley, S. E. 1995, ApJ, 454, 895
Hamilton, A. J. S., & Fesen, R. A. 1991, in Supernovae, 10th Santa Cruz Summer Workshop in Astronomy and Astrophysics, ed. S. E. Woosley (Berlin: Springer), 656
Hamilton, A. J. S., & Fesen, R. A. 2000, ApJ, 542, 779
Hillebrandt, W., Kromer, M., Röpke, F. K., & Ruiter, A. J. 2013, FrPhy, 8, 116
Hillebrandt, W., & Niemeyer, J. C. 2000, ARA&A, 38, 191
Höflich, P., Dragulin, P., Mitchell, J., et al. 2013, FrPhy, 8, 144
Höflich, P., Gerardy, C. L., Nomoto, K., et al. 2004, ApJ, 617, 1258
Höflich, P., & Khokhlov, A. 1996, ApJ, 457, 500
Höflich, P., Khokhlov, A., & Wheeler, J. C. 1995, ApJ, 444, 211
Höflich, P., & Stein, J. 2002, ApJ, 568, 771
Höflich, P., Wheeler, J. C., & Thielemann, F. K. 1998, ApJ, 495, 617
Hofmann, F., Pietsch, W., Henze, M., et al. 2013, A&A, 555, A65
Howell, D. A. 2011, NatCo, 2, 350
Hoyle, F., & Fowler, W. A. 1960, ApJ, 132, 565
Iben, I., Jr, & Tutukov, A. V. 1984, ApJS, 54, 335
Isern, J., Hernanz, M., & José, J. 2011, Lecture Notes in Physics, Vol. 812 (Berlin: Springer), 233
Kaaret, P. 2002, ApJ, 578, 114
Khokhlov, A. M. 1991, A&A, 245, L25
Khokhlov, A. M. 1995, ApJ, 449, 695
Khokhlov, A., Müller, E., & Höflich, P. 1993, A&A, 270, 223
Kromer, M., Fink, M., Stanishev, V., et al. 2013, MNRAS, 429, 2287
Larsson, J., Fransson, C., Kjaer, K., et al. 2013, ApJ, 768, 89
Li, W., Filippenko, A. V., Chornock, R., et al. 2003, PASP, 115, 453L
Li, W., Leaman, J., Chornock, R., et al. 2011, MNRAS, 412, 1441
Livne, E. 1999, ApJL, 527, L97
Livne, E., Asida, S. M., & Höflich, P. 2005, ApJ, 632, 443
Maeda, K., Taubenberger, S., Sollerman, J., et al. 2010, ApJ, 708, 1703
McConnachie, A. W., Irwin, M. J., Ferguson, A. M. N., et al. 2005, MNRAS, 356, 979
Morton, D. C. 1991, ApJS, 77, 119
Niemeyer, J. C., & Hillebrandt, W. 1995, ApJ, 452, 779
Niemeyer, J. C., Hillebrandt, W., & Woosley, S. E. 1996, ApJ, 471, 903
Nomoto, K. 1982, ApJ, 253, 798
Nomoto, K., Thielemann, F.-K., & Yokoi, K. 1984, ApJ, 286, 644
Nomoto, K., Uenishi, T., Kobayashi, C., et al. 2003, in From Twilight to Highlight: The Physics of Supernovae, ed. W. Hillebrandt, & B. Leibundgut (Berlin: Springer), 115
Nugent, P. E., Sullivan, M., Cenko, S. B., et al. 2011, Natur, 480, 344

Osterbrock, D. E. 2001, Walter Baade A Life in Astrophysics ed. D. E. Osterbrock, 2001 (Princeton, NJ: Princeton Univ. Press), 93
Pakmor, R., Hachinger, S., Röpke, F. K., & Hillebrandt, W. 2011, A&A, 528, A117
Pastorello, A., Mattila, S., Zampieri, L., et al. 2008, MNRAS, 389, 113
Penney, R., & Höflich, P. 2014, ApJ, 795, 84
Perets, H. B., Badenes, C., Arcavi, I., Simon, J. D., & Gal-yam, A. 2011, ApJ, 730, 89
Plewa, T. 2007, ApJ, 657, 942
Quimby, R., Höflich, P., Kannappan, S. J., et al. 2006, ApJ, 636, 400
Reming, I. S., & Khokhlov, A. M. 2014, ApJ, 794, 87
Rasio, F. A., & Shapiro, S. L. 1994, ApJ, 432, 242
Reinecke, M., Hillebrandt, W., & Niemeyer, J. C. 1999, A&A, 347, 739
Reinecke, M., Hillebrandt, W., & Niemeyer, J. C. 2002, A&A, 391, 1167
Röpke, F. K., Hillebrandt, W., Niemeyer, J. C., & Woosley, S. E. 2006, A&A, 448, 1
Röpke, F. K., Kromer, D., Seitenzahl, I. R., et al. 2012, ApJL, 750, L19
Röpke, F. K., Woosley, S. E., & Hillebrandt, W. 2007, ApJ, 660, 1344
Seitenzahl, I. R., Ciaraldi-Schoolmann, F., Röpke, F. K., et al. 2013, MNRAS, 429, 1156
Sjouwerman, L. O., & Dickel, J. R. 2001, in AIP Conf. Ser. 565, Young Supernova Remnants, ed. S. S. Holt, & U. Hwang, 433
Stritzinger, M. D., Hsiao, E., Valenti, S., et al. 2014, A&A, 561, AA146
Sugimoto, D., & Nomoto, K. 1980, SSRv, 25, 155
Timmes, F. X., & Woosley, S. E. 1992, ApJ, 396, 649
Wang, B., & Han, Z. 2012, NewA, 56, 122
Webbink, R. F. 1984, ApJ, 277, 355
Yamaoka, H., Nomoto, K., Shigeyama, T., & Thielemann, F.-K. 1992, ApJL, 393, L55